remote sensing

Article

A Novel Polarization Scattering Decomposition Model and Its Application to Ship Detection

Lu Fang, Ziyuan Yang, Wenxing Mu and Tao Liu *

School of Electronic Engineering, Naval University of Engineering, Wuhan 430033, China; 21101001@nue.edu.cn (L.F.); yzy_199702@sina.com (Z.Y.); 20501001@nue.edu.cn (W.M.)
* Correspondence: liutao1018@hotmail.com

Abstract: In polarimetric synthetic aperture radar (POLSAR), it is of great significance for civil and military applications to find novel model-based decomposition methods suitable for ship detection in different detection backgrounds. Based on the physical interpretation of polarimetric decomposition theory and the Lasso rule for sparse features, we propose a four-component decomposition model, which is composed of surface scattering (Odd), double-bounce scattering (Dbl), volume scattering (Vol), and $\pm 45^{\circ}$ oriented dipole (Od). In principle, the Od component can describe the compounded scattering structure of a ship consisting of odd-bounce and even-bounce reflectors. Moreover, the pocket perceptron learning algorithm (PPLA) and support vector machine (SVM) are utilized to solve the linear inseparable problems in this study. Using large amounts of RADARSAT-2 (RS-2) fully polarized SAR data and AIRSAR data, our experimental results show that the Od component can make a great contribution to ship detection. Compared with other conventional decomposition methods used in the experiments, the proposed four-component decomposition method has better performance and is more effective and feasible to detect ships.

Keywords: polarimetric synthetic aperture radar (POLSAR); ship detection; pocket perceptron linear algorithm (PPLA); model-based scattering power decomposition

check for updates

Citation: Fang, L.; Yang, Z.; Mu, W.; Liu, T. A Novel Polarization Scattering Decomposition Model and Its Application to Ship Detection. *Remote Sens.* **2024**, *16*, 178. https://doi.org/10.3390/rs16010178

Academic Editor: Gerardo Di Martino

Received: 5 November 2023
Revised: 25 December 2023
Accepted: 27 December 2023
Published: 31 December 2023

1. Introduction

Polarimetric synthetic aperture radar (POLSAR) is an advanced microwave remote sensing system and is extensively used in the military and civil fields owing to its unique advantages of all-day all-weather and multi-channel continuous observation. It can acquire not only high-resolution imagery but also the complete electromagnetic scattering characteristics of targets [1–4]. Ship detection in POLSAR imagery plays a vital role in marine monitoring and has attracted enormous attention to help government departments deal with maritime emergencies in a timely manner in recent years.

To the best of our knowledge, ship detectors using POLSAR can be divided into main categories, including the following: (1) independent polarization channel composition [5], (2) polarization optimal [4,6], (3) polarimetric scattering mechanism [7,8], (4) ship wake detection [9], and (5) data-driven or deep learning-based [10–12]. Regarding the polarimetric scattering mechanism, various target decomposition algorithms are used for ship detection. Ringrose et al. used the Cameron coherent target decomposition method to detect ships from spaceborne imaging radar C-band data [13]. Chen et al. proposed a ship-detection method which used polarization cross-entropy as a discriminative parameter [14]. Zhang et al. combined the complete polarimetric covariance difference matrix and the four-component decomposition proposed by Yamaguchi for ship detection [8]. Among these target decomposition algorithms, the model-based scattering property decomposition algorithm has good prospects for application in ship detection because it has strong physical interpretability and can correlate each resolution unit with the corresponding physical scattering mechanism.

The decomposition objects of the model-based decomposition for polarized scattering characteristics include the scattering matrix [15,16], the Kennaugh matrix [17,18], and the coherency or covariance matrix [19–29]. Among these, target decomposition methods using covariance or coherency matrices are the most widely used. These decomposition methods usually assume that some scatterers exist in the scattering target and decompose different scattering models according to different scatterers.

The model-based scattering power decomposition method was first developed by Freeman and Durden [19] around 1998. This three-component decomposition model (FDD) is based on simple physical scattering mechanisms and is built under the reflection symmetry assumption that $\langle S_{HH}S_{HV}^{*} \rangle = 0$ and $\langle S_{HV}S_{VV}^{*} \rangle = 0$. FDD has been successfully applied to the natural distribution regions which satisfy reflection symmetry, and shows good classification results.

To address the non-reflection symmetric case that $\langle S_{HH}S_{HV}^{*} \rangle \neq 0$ and $\langle S_{HV}S_{VV}^{*} \rangle \neq 0$, Yamaguchi et al. [20] added the helix scattering power for the more general scattering mechanism. FDD was extended and a four-component scattering model (Y4O) was proposed in 2005. Furthermore, in Y4O, the volume-scattering component was modified. Y4O is effective in both urban and vegetated areas. However, the polarimetric information is still not utilized completely. It is known that there are nine independent polarimetric parameters in coherency matrices or covariance matrices. In Y4O, six parameters of the covariance matrix are used, and the remaining three parameters are not considered. In order to mitigate or eliminate the above problem of incomplete utilization of polarimetric parameters, many significant improvements have been proposed.

The orientation angle compensation is introduced to the model-based decomposition [21–23]. By rotating the coherency matrix, the number of independent parameters reduced from nine to eight, leaving two unaccounted. In 2013, Singh et al. [24] proposed a new generalized four-component decomposition model (G4U) in which all nine polarimetric parameters have been utilized by performing a set of unitary transformations on the coherency matrix. Compared with other model-based decompositions that existed at that time, G4U was able to improve the image interpretation considerably. Later, the ad hoc procedures for making full use of the polarization information in the coherency matrix were developed [2,25]. In 2018, Singh et al. [26] proposed a six-component decomposition method (6SD) which accounted for the oriented dipole structures. It was shown that 6SD was easier to display the additional relevant information than the decomposition models which existed previously. Similarly, many researchers attempt to improve the scattering models to apply to general scattering cases [27–29]. However, the improved decomposition models became more and more complicated. Since the complexity of the model increases with the number of components, a compromise is made between the complexity and efficiency of the model. It is important to note that we focus on the four-component decomposition model.

This paper intends to propose a four-component decomposition method which is applicable to ship detection in different detection backgrounds. The main contributions of this study are:

(1) Extracting 23-dimensional polarization features from six kinds of conventional polarimetric decomposition methods and using Least Absolute Shrinkage and Selection Operator (Lasso) to select the optimal polarization features. The initial optimal polarization features are Odd, Dbl, Vol, and Od.
(2) Using the Odd, Dbl, Vol, and Od components, we derive a four-component decomposition model from mathematical and theoretical perspectives.
(3) PPLA and SVM are adopted to solve the linearly inseparable problems under low-resolution experimental circumstances. The rationality of our decomposition model is verified using large amounts of RADARSAT-2 data and AIRSAR data.

The organization of this paper is as follows. Section 2 introduces the basic theory of POLSAR and presents a novel four-component decomposition method. In Section 3, the effectiveness of the four-component model is validated using the simulated data and the measured data. Experimental results in comparison with other conventional decomposition methods and the corresponding analysis are also demonstrated in this section. Sections 4 and 5 are the discussion and conclusion, respectively.

2. Materials and Methods

2.1. POLSAR Data Description

In a POLSAR measurement system, each pixel can be represented by a 2×2 complex scattering matrix $[S]$ [30]. The expression is as follows [31].

$$[S] = \begin{bmatrix} S_{HH} & S_{HV} \\ S_{VH} & S_{VV} \end{bmatrix} \tag{1}$$

The horizontally polarized waves and vertically polarized waves are respectively by H and V. S_{HH}, S_{VV}, and S_{HV} are the backscattering coefficients of the HH, VV, and HV polarimetric channels, respectively. When the reciprocity theorem is satisfied, i.e., $S_{HV} = S_{VH}$, the Pauli scattering vector $\mathbf{k}_P$ is obtained as:

$$\mathbf{k}_P = \frac{1}{\sqrt{2}} \begin{bmatrix} S_{HH} + S_{VV} \\ S_{HH} - S_{VV} \\ 2S_{HV} \end{bmatrix} \tag{2}$$

However, in real scenarios, relying only on the scattering matrix cannot describe the full properties of the target. The second-order statistics of the scattering matrix is a better form [32]. Here, we use the coherence matrix which is defined as

$$\langle [T] \rangle = \left\langle \mathbf{k}_p \mathbf{k}_P^{\dagger} \right\rangle = \begin{bmatrix} T_{11} & T_{12} & T_{13} \\ T_{21} & T_{22} & T_{23} \\ T_{31} & T_{32} & T_{33} \end{bmatrix} = \begin{bmatrix} |k_1|^2 & \langle k_1 k_2^* \rangle & \langle k_1 k_3^* \rangle \\ \langle k_2 k_1^* \rangle & |k_2|^2 & \langle k_2 k_3^* \rangle \\ \langle k_3 k_1^* \rangle & \langle k_3 k_2^* \rangle & |k_3|^2 \end{bmatrix} \tag{3}$$

where

$$\mathbf{k}_P = \begin{bmatrix} k_1 \\ k_2 \\ k_3 \end{bmatrix} = \frac{1}{\sqrt{2}} \begin{bmatrix} S_{HH} + S_{VV} \\ S_{HH} - S_{VV} \\ 2S_{HV} \end{bmatrix} \tag{4}$$

where $\langle \cdot \rangle$ denotes the ensemble average in the data processing, $*$ denotes the complex conjugation, and $\dagger$ denotes complex conjugation and transposition [26].

There are two different data formats in model-based POLSAR decomposition, commonly known as the coherency matrix [2,21,23,24,26] and the covariance matrix [19,20,28]. Since these two matrices are frequently used in the data analysis, it is necessary to explain the relation between the two. The covariance matrix and coherency matrix are equivalent mathematically. Therefore, the information contained inside is the same. One should note that we concentrate on decomposing the coherency matrix, whereas for generating simulated data, we use the covariance matrix which is defined as

$$\langle [C] \rangle^{HV} = \begin{bmatrix} \left\langle |S_{HH}|^2 \right\rangle & \sqrt{2} \langle S_{HH} S_{HV}^* \rangle & \langle S_{HH} S_{VV}^* \rangle \\ \sqrt{2} \langle S_{HV} S_{HH}^* \rangle & 2\left\langle |S_{HV}|^2 \right\rangle & \sqrt{2} \langle S_{HV} S_{VV}^* \rangle \\ \langle S_{VV} S_{HH}^* \rangle & \sqrt{2} \langle S_{VV} S_{HV}^* \rangle & \left\langle |S_{VV}|^2 \right\rangle \end{bmatrix} \tag{5}$$

The following equation gives the mutual relations and transformations between covariance matrices and coherency matrices:

$$[T] = [U_P][C][U_P]^{\dagger},\ [C] = [U_P]^{\dagger}[T][U_P] \tag{6}$$

where

$$[U_P] = \frac{1}{\sqrt{2}}\begin{bmatrix} 1 & 0 & 1 \\ 1 & 0 & -1 \\ 0 & \sqrt{2} & 0 \end{bmatrix} \tag{7}$$

As a summary, the mutual transformation of various polarization matrices can be visualized as shown in Figure 1.

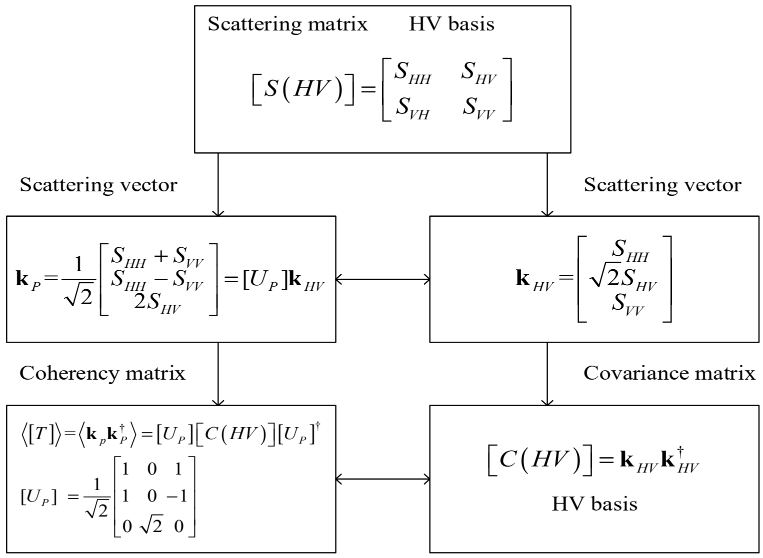

Figure 1. Mutual transformation of polarization matrices.

2.2. A Novel Polarimetric Decomposition Model

Applying model-based polarimetric decomposition algorithms to detect ships from sea clutter has been less studied, and existing model-based polarimetric decomposition algorithms focus on interpreting terrestrial vegetation and cities. Inspired by the Lasso rule of feature selection, we attempt to select the principal features applicable to ship detection from six kinds of conventional polarimetric decomposition methods introduced above. After statistical analysis, we find that the results of the four features extracted are basically consistent with those of all features utilized in the experiments, and then a novel polarimetric decomposition model is proposed, which is suitable for ship detection.

2.2.1. Lasso

Lasso, short for Least Absolute Shrinkage and Selection Operator, was first proposed by Robert Tibshiran in 1996 [33]. It is a linear regression method using L1-regularization. When L1 regularization is adopted, the weights of some less important features will be zero, thus achieving sparse feature and feature selection.

For data $\left(\mathbf{X}^i, y_i\right)$, $i = 1, 2, \ldots N$, $\mathbf{X}^i = \left(x_{i1}, \ldots x_{ip}\right)^T$ are the predictor variables, and y_i are the responses, $\sum_i x_{ij}/N = 0$, $\sum_i x_{ij}^2/N = 1$.

Letting $\hat{\beta} = \left(\hat{\beta}_1, \ldots \hat{\beta}_p\right)^T$, the Lasso estimate $\left(\alpha, \hat{\beta}\right)$ is defined by

$$\left(\hat{\alpha}, \hat{\beta}\right) = \operatorname{argmin} \sum_{i=1}^{N} \left(y_i - \alpha - \sum_j \beta_j x_{ij}\right)^2 \quad \text{subject to} \sum_j \left|\beta_j\right| \le t \tag{8}$$

Here $t \ge 0$ is a tuning parameter which can control the shrinkage applied to the estimates. Let $t_0 = \sum \left|\hat{\beta}_j^{\circ}\right|$. Values of $t < t_0$ will cause shrinkage of the solutions towards zero, and some coefficients may be exactly zero [33]. Figure 2 is the estimation picture for the Lasso. It is clear from Figure 2 that Lasso can produce coefficients equal to zero.

$$\sum_{i=1}^{N}\left(y_i - \sum_j \beta_j x_{ij}\right)^2 = \left(\beta - \overset{\wedge}{\beta^{\circ}}\right)^T \mathbf{X}^T\mathbf{X}\left(\beta - \overset{\wedge}{\beta^{\circ}}\right) \tag{9}$$

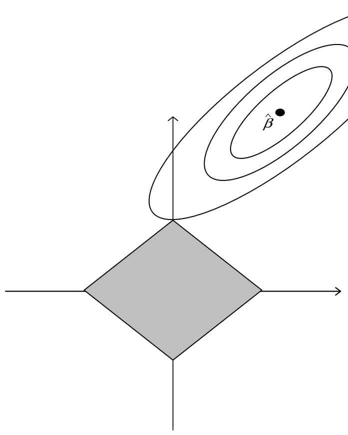

Figure 2. Estimation picture for the Lasso.

The solid curves indicate the elliptical contours of this function; the rotated square indicates the constraint region. The Lasso solution is the first place that the contours touch the square. In Figure 2, this will occur at a corner, corresponding to a zero coefficient [33].

2.2.2. Optimal Polarization Features Selection

In this paper, six kinds of polarimetric decomposition methods, including FDD in 1998, Y4O in 2005, An decomposition in 2010, G4U in 2013, Cui decomposition in 2014, and 6SD in 2018 were used to extract 23-dimensional polarization features. The parameters extracted using different polarimetric decomposition methods are listed in Table 1. Then, the optimal polarization features selection was performed using the Lasso method. Table 2 shows the ranking of the 23 features in terms of importance. After the selection analysis, four better polarization features, i.e., Odd-FDD, Dbl-FDD, Vol-An, and Od-6SD were obtained. The specific data and experimental comparison results are presented in the experimental section.

Table 1. Parameters extracted using different polarization decomposition methods.

Decomposition Methods	Decomposition Parameters	Description
FDD	Odd-FDD, Dbl-FDD, Vol-FDD	Freeman-Duren decomposition in 1998: surface scattering component, double-bounce scattering component, and volume scattering component
Y4O	Odd-Y4O, Dbl-Y4O, Vol-Y4O, Hlx-Y4O	Yamaguchi decomposition in 2005: surface scattering component, double-bounce scattering component, volume scattering component, and helix scattering component
An decomposition	Odd-An, Dbl-An, Vol-An	An decomposition in 2010: surface scattering component, double-bounce component, and volume scattering component

Table 1. *Cont.*

Decomposition Methods	Decomposition Parameters	Description
G4U	Odd-G4U, Dbl-G4U, Vol-G4U, Hlx-G4U	G4U decomposition in 2013: surface scattering component, double-bounce scattering component, volume scattering component, and helix scattering component
Cui decomposition	Odd-Cui, Dbl-Cui, Vol-Cui	Cui decomposition in 2014: surface scattering component, double-bounce scattering component, and volume scattering component
6SD	Odd-6SD, Dbl-6SD, Vol-6SD, Hlx-6SD, Od-6SD, Cd-6SD	6SD decomposition in 2018: surface scattering component, double-bounce scattering component, volume scattering component, helix scattering component, oriented dipole scattering component, and compound dipole scattering component

Table 2. The rank of the importance of 23 features.

Features	Ranking
Odd-FDD	1
Dbl-FDD	2
Vol-An	3
Od-6SD	4
Vol-FDD	5
Odd-Y4O	6
Cd-6SD	7
Vol-G4U	8
Vol-6SD	9
Vol-Y4O	10
Dbl-Cui	11
Odd-An	12
Hlx-6SD	13
Vol-Cui	14
Dbl-6SD	15
Dbl-G4U	16
Odd-G4U	17
Dbl-An	18
Dbl-Y4O	19
Hlx-Y4O	20
Hlx-G4U	21
Odd-Cui	22
Odd-6SD	23

2.2.3. A Four-Component Decomposition Model for Ship Detection

The proposed four-component decomposition model comprises the Odd, Dbl, Vol, and Od components. Next, we analyze these four scattering components.

Each component can be represented by a composite scattering matrix as follows:

(1) Odd:

$$[S]_s^{\text{total}} = \frac{1}{2}\begin{bmatrix} 1 & 0 \\ 0 & 1 \end{bmatrix},\ \mathbf{k}_P = \frac{1}{\sqrt{2}}\begin{bmatrix} 1 \\ 0 \\ 0 \end{bmatrix}$$

$$[T]_s = \begin{bmatrix} 1 & 0 & 0 \\ 0 & 0 & 0 \\ 0 & 0 & 0 \end{bmatrix} \Rightarrow [T]_s = \begin{bmatrix} 1 & \beta^* & 0 \\ \beta & |\beta|^2 & 0 \\ 0 & 0 & 0 \end{bmatrix} \tag{10}$$

(2) Dbl:

$$[S]_d^{\text{total}} = \frac{1}{2}\begin{bmatrix} 1 & 0 \\ 0 & -1 \end{bmatrix},\ \mathbf{k}_P = \frac{1}{\sqrt{2}}\begin{bmatrix} 0 \\ 1 \\ 0 \end{bmatrix}$$

$$[T]_d = \begin{bmatrix} 0 & 0 & 0 \\ 0 & 1 & 0 \\ 0 & 0 & 0 \end{bmatrix} \Rightarrow [T]_d = \begin{bmatrix} |\alpha|^2 & \alpha & 0 \\ \alpha^* & 1 & 0 \\ 0 & 0 & 0 \end{bmatrix} \tag{11}$$

(3) Vol:

There are various volume scattering models proposed. We adopt the volume scattering model proposed by An et al., which gives the maximum entropy.

$$[T]_{vol} = \frac{1}{3}\begin{bmatrix} 1 & 0 & 0 \\ 0 & 1 & 0 \\ 0 & 0 & 1 \end{bmatrix} \tag{12}$$

(4) Od:

The Od component describes the composite scattering structure consisting of even-bounce and odd-bounce reflectors. There are many upright metal parts on the ship deck, similar to a steel frame structure (even-bounce reflector), and these can form a composite scattering structure with the deck (odd-bounce reflector). As analyzed in [26], these complex scatterings can be represented by a $\pm 45^\circ$ oriented dipole component complex scattering matrix.

The scattering characteristics of an oriented dipole depend significantly on the target orientation with respect to the polarization coordinate system. Suppose we have two dipoles which are oriented at 45° and -45° against each other, as illustrated in Figure 3. The corresponding scattering submatrices are given in the following equations:

$$[S]_{\text{dipole}}^{45^\circ} = \begin{bmatrix} 1 & 1 \\ 1 & 1 \end{bmatrix},\ [S]_{\text{dipole}}^{-45^\circ} = \begin{bmatrix} 1 & -1 \\ -1 & 1 \end{bmatrix} \tag{13}$$

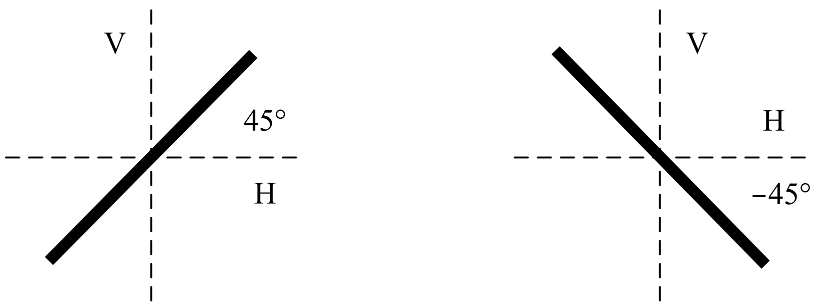

Figure 3. $\pm 45^\circ$ oriented dipole.

By combining the scattering matrix of an odd-bounce reflector with the scattering matrix of a $\pm 45^\circ$ oriented dihedral, a composite-oriented dipole scattering matrix is formed [26]:

$$
\begin{aligned}
&\Re(T_{13}) > 0\\
&[S]^{45^\circ}_{\text{dipole}} = \tfrac{1}{2}\begin{bmatrix}1 & 1\\ 1 & 1\end{bmatrix},\ \mathbf{k}_P = \tfrac{1}{\sqrt{2}}\begin{bmatrix}1\\0\\1\end{bmatrix}\\
&[T]^{45^\circ}_{\text{dipole}} = \tfrac{1}{2}\begin{bmatrix}1 & 0 & 1\\ 0 & 0 & 0\\ 1 & 0 & 1\end{bmatrix}
\end{aligned} \tag{14}
$$

$$
\begin{aligned}
&\Re(T_{13}) < 0\\
&[S]^{-45^\circ}_{\text{dipole}} = \tfrac{1}{2}\begin{bmatrix}1 & -1\\ -1 & 1\end{bmatrix},\ \mathbf{k}_P = \tfrac{1}{\sqrt{2}}\begin{bmatrix}1\\0\\-1\end{bmatrix}\\
&[T]^{-45^\circ}_{\text{dipole}} = \tfrac{1}{2}\begin{bmatrix}1 & 0 & -1\\ 0 & 0 & 0\\ -1 & 0 & 1\end{bmatrix}
\end{aligned} \tag{15}
$$

2.2.4. The Procedure of The Proposed Four-Component Decomposition Model

$$
\begin{aligned}
T &= f_{\text{s}}\begin{bmatrix}1 & \beta^* & 0\\ \beta & |\beta|^2 & 0\\ 0 & 0 & 0\end{bmatrix} + f_{\text{d}}\begin{bmatrix}|\alpha|^2 & \alpha & 0\\ \alpha^* & 1 & 0\\ 0 & 0 & 0\end{bmatrix} + \tfrac{P_{\text{v}}}{3}\begin{bmatrix}1 & 0 & 0\\ 0 & 1 & 0\\ 0 & 0 & 1\end{bmatrix} + f_{\text{od}}\begin{bmatrix}1 & 0 & \pm 1\\ 0 & 0 & 0\\ \pm 1 & 0 & 1\end{bmatrix}\\
&= \tfrac{P_{\text{s}}}{1+|\beta|^2}\begin{bmatrix}1 & \beta^* & 0\\ \beta & |\beta|^2 & 0\\ 0 & 0 & 0\end{bmatrix} + \tfrac{P_{\text{d}}}{1+|\alpha|^2}\begin{bmatrix}|\alpha|^2 & \alpha & 0\\ \alpha^* & 1 & 0\\ 0 & 0 & 0\end{bmatrix} + \tfrac{P_{\text{v}}}{3}\begin{bmatrix}1 & 0 & 0\\ 0 & 1 & 0\\ 0 & 0 & 1\end{bmatrix} + \tfrac{P_{\text{od}}}{2}\begin{bmatrix}1 & 0 & \pm 1\\ 0 & 0 & 0\\ \pm 1 & 0 & 1\end{bmatrix}
\end{aligned} \tag{16}
$$

The flowchart of the proposed decomposition is shown in Figure 4. P_{s} denotes the power of Odd component; P_{d} indicates the power of Dbl component; P_{v} denotes the power of Vol component; and P_{od} indicates the power of Od component. The superscript indicates the element of the coherence matrix after rotation. The details will be illustrated as follows.

$$
\begin{cases}
T'_{11} = \frac{P_{\text{s}}}{1+|\beta|^2} + \frac{P_{\text{d}}}{1+|\alpha|^2}|\alpha|^2 + \frac{P_{\text{v}}}{3} + \frac{P_{\text{od}}}{2}\\
T'_{12} = \frac{P_{\text{s}}}{1+|\beta|^2}\beta^* + \frac{P_{\text{d}}}{1+|\alpha|^2}\alpha\\
T'_{13} = \frac{P_{\text{od}}}{2}\\
T'_{22} = \frac{P_{\text{s}}}{1+|\beta|^2}|\beta|^2 + \frac{P_{\text{d}}}{1+|\alpha|^2} + \frac{P_{\text{v}}}{3}\\
T'_{33} = \frac{P_{\text{v}}}{3} + \frac{P_{\text{od}}}{2}
\end{cases} \tag{17}
$$

According to [26], we can directly obtain the power of the Od

$$P_{od} = 2|\Re(T_{13})| \tag{18}$$

where $\Re$ denotes real part.

We solve the remaining unknowns according to the solution method in [21]. P_{v} is determined by the smaller of T'_{11} and T'_{33}

$$P_{\text{v}} = \min\left(3T'_{11},\ 3T'_{33}\right) \tag{19}$$

where $\min(\cdot)$ denotes the smaller one.

Hence, the first operation is to check whether T'_{11} is less than T'_{33} or not. If T'_{11} is less than or equal to T'_{33}, both P_{s} and β are zero, and the power of double-bounce scattering is expressed as

$$P_{\text{d}} = T'_{22} + T'_{33} - 2T'_{11} - 2\left|\Re\left(T'_{13}\right)\right| \tag{20}$$

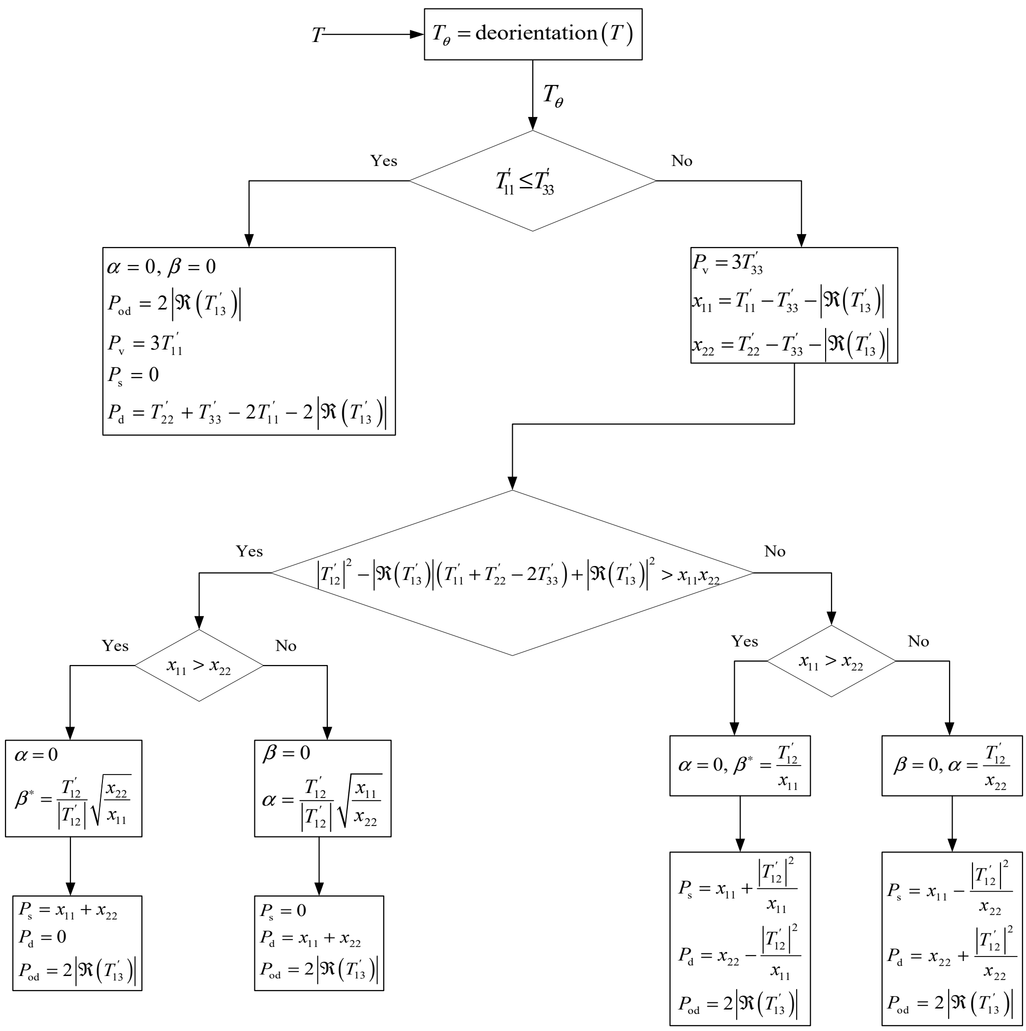

Figure 4. The proposed decomposition flow chart.

If T'_{11} is greater than T'_{33}, after the subtraction of volume scattering, x_{11} and x_{22} are represented as follows:

$$x_{11} = T'_{11} - T'_{33} - \left|\Re\left(T'_{13}\right)\right|,\ x_{22} = T'_{22} - T'_{33} - \left|\Re\left(T'_{13}\right)\right| \tag{21}$$

The second operation is to check whether $\left|T'_{12}\right|^2 - \left|\Re\left(T'_{13}\right)\right|\left(T'_{11} + T'_{22} - 2T'_{33}\right) + \left|\Re\left(T'_{13}\right)\right|^2$ is greater than the product of x_{11} and x_{22} or not.

Under the condition of $\left|T'_{12}\right|^2 - \left|\Re\left(T'_{13}\right)\right|\left(T'_{11} + T'_{22} - 2T'_{33}\right) + \left|\Re\left(T'_{13}\right)\right|^2 > x_{11}x_{22}$, if x_{11} is greater than x_{22}, the remaining unknown part is surface scattering, and

$$\alpha = 0,\ \beta^* = \frac{T'_{12}}{\left|T'_{12}\right|}\sqrt{\frac{x_{22}}{x_{11}}},\ P_s = x_{11} + x_{22},\ P_d = 0,\ P_{od} = 2\left|\Re\left(T'_{13}\right)\right| \tag{22}$$

Otherwise, the remaining unknown part is double-bounce scattering, and

$$\alpha = \frac{T'_{12}}{\left|T'_{12}\right|}\sqrt{\frac{x_{11}}{x_{22}}},\ \beta = 0,\ P_s = 0,\ P_d = x_{11} + x_{22},\ P_{od} = 2\left|\Re\left(T'_{13}\right)\right| \tag{23}$$

Similarly, if $\left|T_{12}'\right|^2 - \left|\Re\left(T_{13}'\right)\right|\left(T_{11}' + T_{22}' - 2T_{33}'\right) + \left|\Re\left(T_{13}'\right)\right|^2 \leq x_{11}x_{22}$, it is necessary to check whether x_{11} is greater than x_{22} or not. If x_{11} is greater than x_{22}, α is set to zero. Otherwise, β is set to zero. P_s, P_d, P_{od}, α, and β are shown as follows:

$$\text{if } (x_{11} > x_{22})\ \beta^* = \frac{T_{12}'}{x_{11}},\ P_s = x_{11} + \frac{\left|T_{12}'\right|^2}{x_{11}},\ P_d = x_{22} - \frac{\left|T_{12}'\right|^2}{x_{11}},\ P_{od} = 2\left|\Re\left(T_{13}'\right)\right| \tag{24}$$

$$\text{else } \alpha = \frac{T_{12}'}{x_{22}},\ P_s = x_{11} - \frac{\left|T_{12}'\right|^2}{x_{22}},\ P_d = x_{22} + \frac{\left|T_{12}'\right|^2}{x_{22}},\ P_{od} = 2\left|\Re\left(T_{13}'\right)\right| \tag{25}$$

The proposed decomposition model satisfies the following equation:

$$Span = P_s + P_d + P_v + P_{od} \tag{26}$$

where $P_s \geq 0,\ P_d \geq 0,\ P_v \geq 0, P_{od} \geq 0$.

2.3. Pocket Perceptron Learning Algorithm (PPLA)

In real scenarios, PPLA is generally used to address linearly inseparable problems. The essence of PPLA is to identify mistakes and make them right. The algorithm is presented in Table 3.

Table 3. PPLA.

(1) Input the fully polarimetric sample data set $\mathbf{X} = (\mathbf{x_1}, \mathbf{x_2} \cdots \mathbf{x_i} \cdots \mathbf{x_n})$. The sample data have 9 features, denoted by vector $\mathbf{x_i}$, $\mathbf{x_i} = (x_{i1}, x_{i2}, x_{i3}, x_{i4}, x_{i5}, x_{i6}, x_{i7}, x_{i8}, x_{i9})^{\mathbf{T}}$. Label set $(y_1, y_2, y_3 \cdots y_n), y_i \in \{0,1\}$. Note that $y = 1$ here denotes target, $y = 0$ denotes clutter. The maximum number of iterations is n_max.
(2) Initial weight $\mathbf{w}$ and bias b are selected randomly. Registers $\mathbf{w}_{\text{poc}}$ and b_{poc} store the optimal solution in the current training times.
(3) For $\mathbf{x_i}$, compute $sign(\mathbf{w} \cdot \mathbf{x_i} + b)$, if $sign(\mathbf{w} \cdot \mathbf{x_i} + b) \neq y_i$, then correct $\mathbf{w}$. If the new $\mathbf{w}$ makes fewer mistakes than before, $\mathbf{w} = \mathbf{w} + y_i \cdot \mathbf{x_i}$, until all training examples are correctly classified or the maximum number of iterations is reached.
(4) Output $\mathbf{w}_{\text{poc}}$ and b_{poc}.

2.4. Support Vector Machine (SVM)

SVM is a classifier algorithm in machine learning. It separates two or more classes of data by an optimal or best hyperplane.

In SVM, the input is the fully polarimetric sample data set $\mathbf{X} = (\mathbf{x_1}, \mathbf{x_2} \cdots \mathbf{x_i} \cdots \mathbf{x_n})$, which is the same as in PPLA. Label $y_i \in \{0,1\},\ i = 1, 2, \cdots, n$. The sample data have 9 features, denoted by vector $\mathbf{x_i}$, $\mathbf{x_i} = (x_{i1}, x_{i2}, x_{i3}, x_{i4}, x_{i5}, x_{i6}, x_{i7}, x_{i8}, x_{i9})^{\mathbf{T}}$. By using SVM, the hyperplane $\mathbf{w} \cdot \mathbf{x_i} + b = 0$ and classification decision function $sign(\mathbf{w} \cdot \mathbf{x_i} + b)$ are obtained.

3. Results

3.1. Simulated Data Generation

It is well known that the core of ship detection lies in the ship-sea difference. Considering the difference in the scattering mechanisms between the ship and sea, we utilize the product models and the Monte Carlo method in the literature [34] to generate simulated data. In low-resolution cases, it is difficult to detect targets and clutter with low TCR due to the similar intensity. In high-resolution cases, clutter and targets are generally easier to separate, and detection may occur even with very low TCR.

In light of the literature [35,36], three common statistical models are used with the polarimetric covariance matrix $\mathbf{\Sigma}_C$. Targets are generated from the covariance matrix $\mathbf{\Sigma}_T$. The statistical model of targets is the Wishart or $\mathcal{G}_0$-distribution. Polarimetric covariance matrices were drawn from RADARSAT-2 data [35,36]. Training samples N and test samples testN are 10 000 respectively. The parameter settings are shown in Table 4.

Table 4. Parameter settings of simulated data.

Simulated Data	Distribution	Shape Parameters
Clutter	Wishart	$\mathbf{\Sigma}_C$
	$\mathcal{K}$-distribution	10
	$\mathcal{G}_0$-distribution	10
Ship targets (Low-resolution)	Wishart	$(\mathbf{\Sigma}_T - \mathbf{\Sigma}_C)/\mathrm{tr}(\mathbf{\Sigma}_T - \mathbf{\Sigma}_C) \times \mathrm{TCR}{+}\mathbf{\Sigma}_C$
	$\mathcal{G}_0$-distribution	2
Ship targets (High-resolution)	Wishart	$(\mathbf{\Sigma}_T - \mathbf{\Sigma}_C)/\mathrm{tr}(\mathbf{\Sigma}_T - \mathbf{\Sigma}_C) \times \mathrm{TCR}$
	$\mathcal{G}_0$-distribution	2

In the experiments, L was the multilook number and was set to 4. When the statistical model of clutter was $\mathcal{K}$-distribution or $\mathcal{G}_0$-distribution, the shape parameter was 10. When the statistical model of ship targets was $\mathcal{G}_0$-distribution, the shape parameter was 2.

In low-resolution cases, the TCR is

$$\mathrm{TCR} = \mathrm{tr}(\mathbf{\Sigma}_T - \mathbf{\Sigma}_C)/\mathrm{tr}(\mathbf{\Sigma}_C) \tag{27}$$

where $\mathrm{tr}(\mathbf{\Sigma}_T)$ denotes the power in the low-resolution cases, $\mathrm{tr}(\mathbf{\Sigma}_C)$ denotes the clutter power, and the TCR is 0.5.

In high-resolution cases, the TCR is defined as

$$\mathrm{TCR} = \mathrm{tr}(\mathbf{\Sigma}_t)/\mathrm{tr}(\mathbf{\Sigma}_C) \tag{28}$$

where $\mathrm{tr}(\mathbf{\Sigma}_t)$ denotes the power of the pure targets, and the TCR is still 0.5.

3.2. Measured Data Description

The first fully polarized scene is the North Sea region acquired by RS-2 in November 2013 [35]. The dataset format is of the SLC form, covering a square of 25 × 25 km. A slant range resolution is 5.2 m and azimuth resolution is 7.6 m. There are eleven ships in the scene, as shown in Figure 5a. The yellow rectangle represents a large ship, while the yellow circle represents a small ship. The wind speed is about 16 m/s, signifying the sea state is high [35].

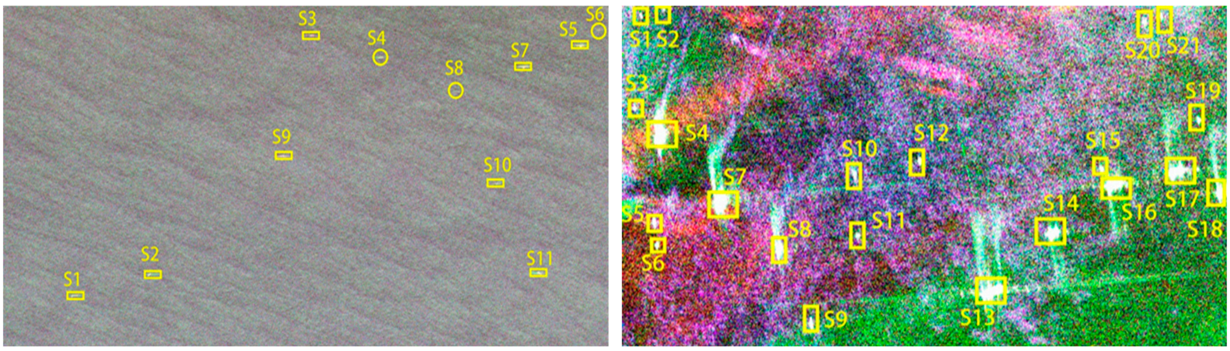

(**a**) (**b**)

Figure 5. Measured images. (**a**) North Sea area in RS-2 image; (**b**) Kojimawan area in AIRSAR image.

The second measured scene is the Kojimawan area in Japan acquired by AIRSAR on 4 October 2000. The scene we used is in the L-band and presents 21 ships, as indicated in Figure 5b. The wind speed is about 12.5 m/s, the sea state is moderate-to-high [37]. Please visit https://vertex.daac.asf.alaska.edu/ (accessed on 4 November 2023) for more information.

3.3. Discussion on The Results of Simulated Experiments

The receiver operating characteristic (ROC) curves of detectors in different scenes are presented in Figures 6–9. "Pd" is the probability of detection and "Pfa" means the PFA. In "CWTW", "C" stands for the clutter, "T" stands for targets, and "W" stands for Wishart distributed. "CWTW" denotes both targets and clutter are Wishart distributed. In "CKTG", "K" represents $\mathcal{K}$-distributed, and "G" represents $\mathcal{G}_0$-distributed. "CKTG" denotes that the clutter is $\mathcal{K}$-distributed and the targets are $\mathcal{G}_0$-distributed. The other two are the same, and will not be repeated here.

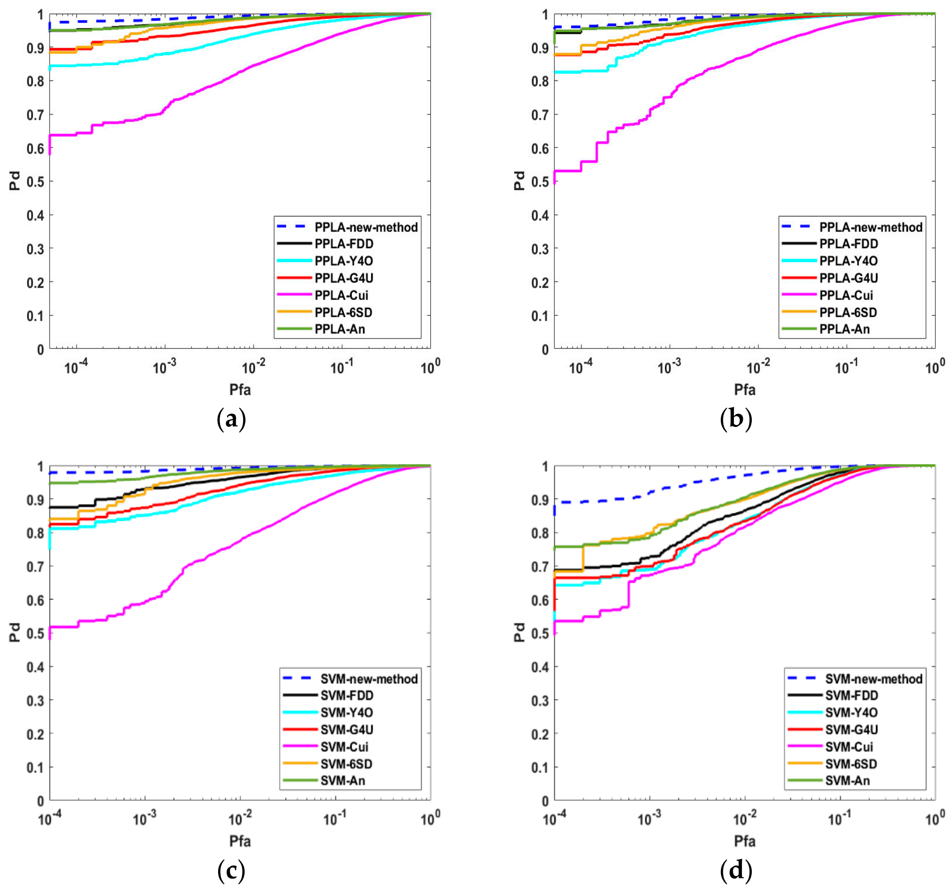

Figure 6. ROC curves with CWTW. (**a**) ROC curves of different decomposition methods using PPLA (low-resolution); (**b**) ROC curves of different decomposition methods using PPLA (high-resolution); (**c**) ROC curves of different decomposition methods using SVM (low-resolution); (**d**) ROC curves of different decomposition methods using SVM (high-resolution).

As shown in Figure 6, in the CWTW scenes, each polarization scattering decomposition model can obtain excellent detection results and the proposed four-component decomposition achieves the best performance. Figure 7 shows the ROC curves in the CWTG case. In both CWTW and CWTG, the clutter is homogeneous, and only the targets obey a different distribution. Figures 8 and 9 are the ROC curves in CKTG and CGTG scenes, respectively. In complex sea environments, the clutter deviates from the Wishart distribution. These two scenes simulate target detection under complex conditions. It can be observed that the probability of detection in CKTG and CGTG scenes is lower than that in CWTW and CWTG scenes.

In order to analyze the relationship between the power proportion of each decomposition component and PPLA weight, the experiments were carried out on the simulated data in scene CKTG. The visualization decomposition results are presented in Figures 10 and 11. Scattering powers are color-coded, with red representing P_d, green representing P_v, and blue representing P_s. Figure 10a shows the Pseudo-Color image of targets; Figure 11a shows the Pseudo-Color image of clutter; Figures 10c and 11c intuitively show the decomposition result of scattering power P_{od}. In Figures 10 and 11, as can be seen, the distribution of clutter and targets is different, which means we can perform the component's power comparison and weight analysis.

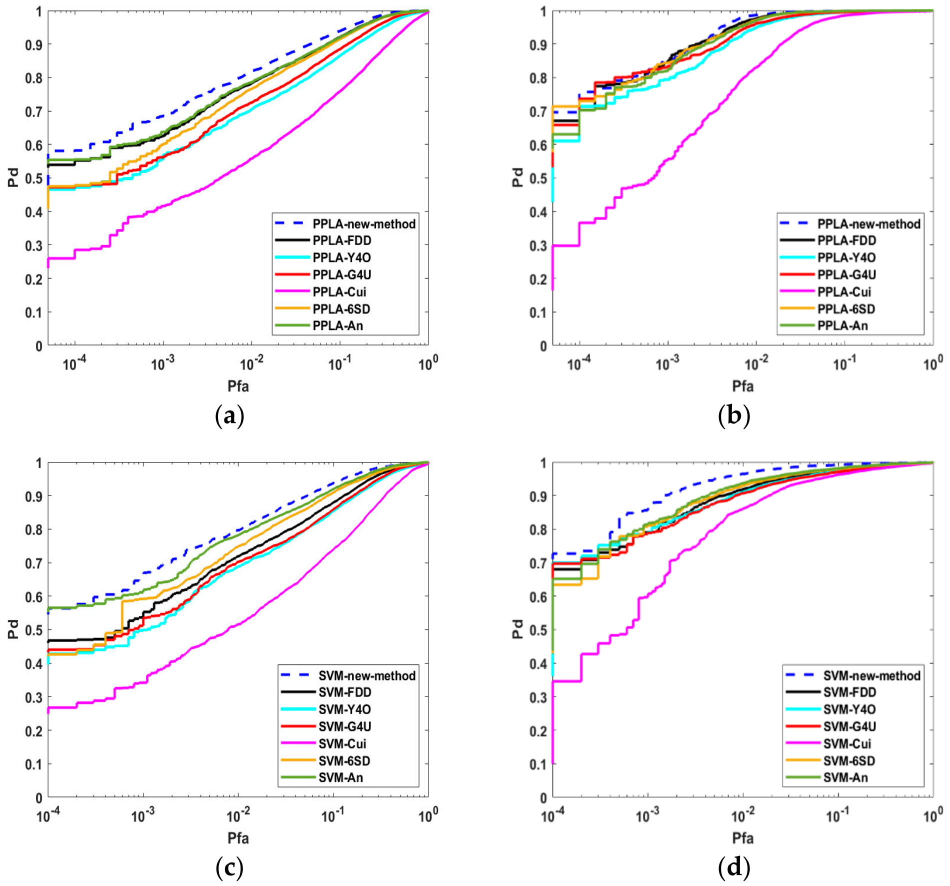

Figure 7. ROC curves with CWTG. (**a**) ROC curves of different decomposition methods using PPLA (low-resolution); (**b**) ROC curves of different decomposition methods using PPLA (high-resolution); (**c**) ROC curves of different decomposition methods using SVM (low-resolution); (**d**) ROC curves of different decomposition methods using SVM (high-resolution).

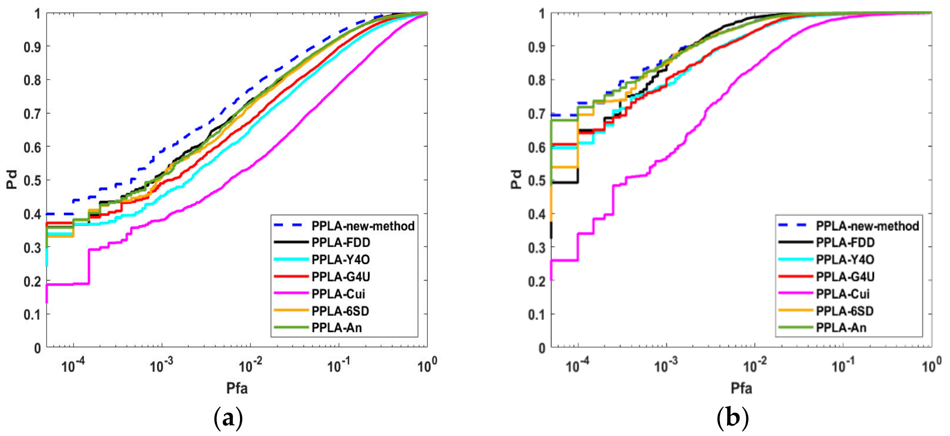

Figure 8. *Cont.*

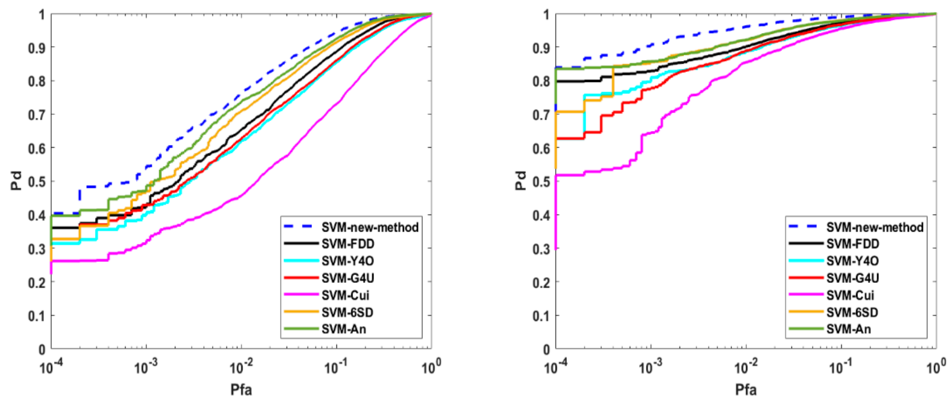

(c) (d)

Figure 8. ROC curves with CKTG. (**a**) ROC curves of different decomposition methods using PPLA (low-resolution); (**b**) ROC curves of different decomposition methods using PPLA (high-resolution); (**c**) ROC curves of different decomposition methods using SVM (low-resolution); (**d**) ROC curves of different decomposition methods using SVM (high-resolution).

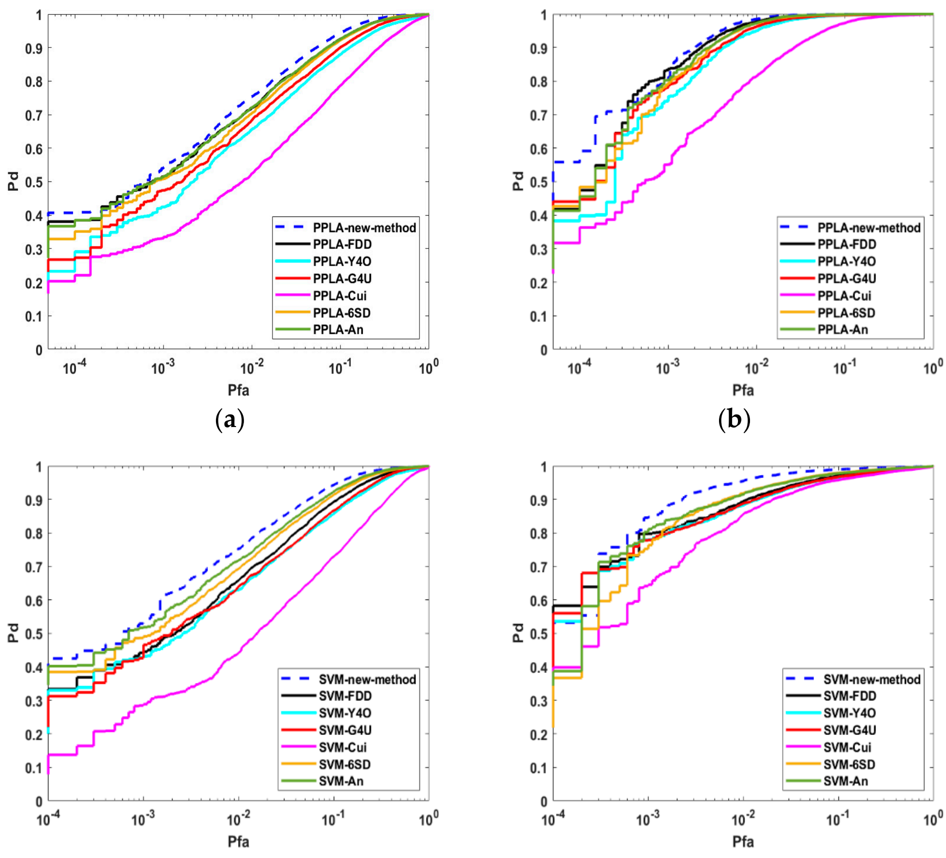

(a) (b)

(c) (d)

Figure 9. ROC curves with CGTG. (**a**) ROC curves of different decomposition methods using PPLA (low-resolution); (**b**) ROC curves of different decomposition methods using PPLA (high-resolution); (**c**) ROC curves of different decomposition methods using SVM (low-resolution); (**d**) ROC curves of different decomposition methods using SVM (high-resolution).

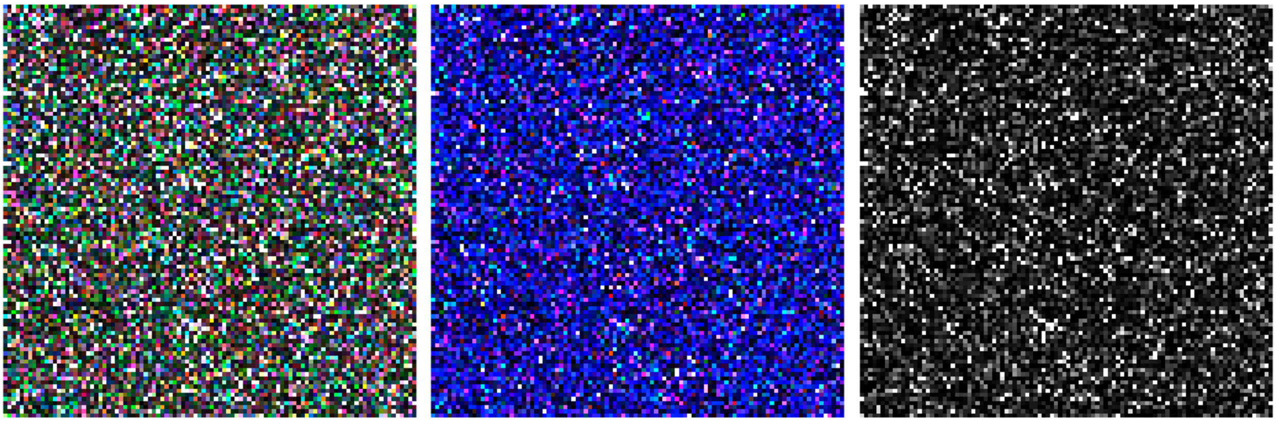

(**a**) (**b**) (**c**)

Figure 10. Pseudo-Color image of decomposing targets in scene CKTG. (**a**) Pseudo-Color image of the decomposing targets; (**b**) The RGB color-codes: blue: Odd, green: Vol, red: Dbl; (**c**) Scattering power P_{od}.

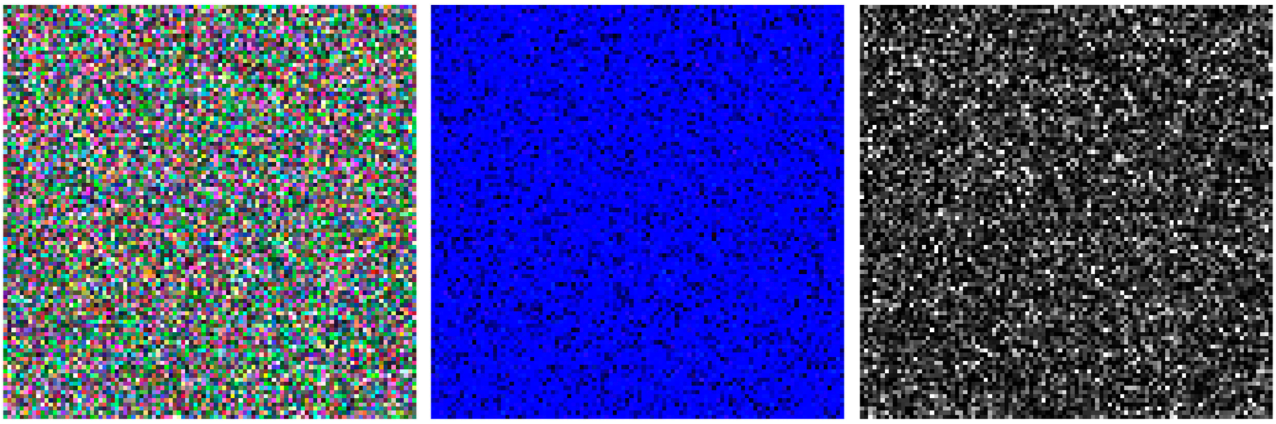

(**a**) (**b**) (**c**)

Figure 11. Pseudo-Color image of decomposing clutter in scene CKTG. (**a**) Pseudo-Color image of decomposing clutter; (**b**) The RGB color-codes: blue: Odd, green: Vol, red: Dbl; (**c**) Scattering power P_{od}.

Figure 12 reveals the relationship between the normalized relative ratio of targets and the normalized PPLA weight in the simulation data. The specific values are listed in Table 5. It can be seen from Figure 12 and Table 5 that the larger the relative ratio of targets, the greater the weight of PPLA.

Table 5. The percentage and PPLA weight of each component's power in simulated data.

Scattering Power	P_{v}	P_{s}	P_{d}	P_{od}
Targets decomposition percentage	11.9393%	66.6104%	11.9939%	9.4564%
Clutter decomposition percentage	3.3121%	88.9883%	2.5796%	5.1200%
Relative ratio of targets (normalization)	0.7322	0	1	0.2816
PPLA weight (normalization)	0.6850	0	1	0.0375

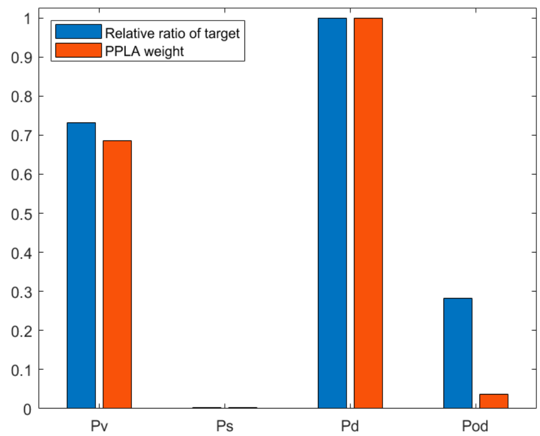

Figure 12. PPLA weight and relative ratio of targets in simulated data.

3.4. Discussion on The Results of Measured Experiments

3.4.1. Validation on RS-2 Dataset

The ROC curves of different decomposition methods are shown in Figure 13. Tables 6 and 7 independently present the AUC of PPLA and the AUC of SVM. The results are consistent with those of the simulated experiments. The proposed four-component decomposition method achieves the best performance. PPLA and SVM have the similar trends.

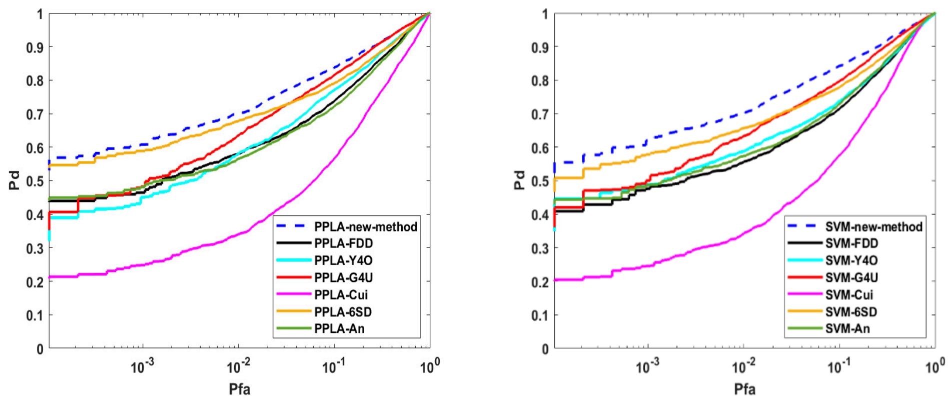

Figure 13. ROC curves of different decomposition methods in the RS-2 image. (**a**) ROC curves of PPLA; (**b**) ROC curves of SVM.

Table 6. AUC of PPLA.

PPLA	AUC
new method	0.9305
G4U	0.9247
6SD	0.9106
Y4O	0.9019
FDD	0.8919
An	0.8852
Cui	0.8124

Table 7. AUC of SVM.

SVM	AUC
new method	0.9319
G4U	0.9185
6SD	0.9055
An	0.8895
Y4O	0.8871
FDD	0.8822
Cui	0.8332

3.4.2. Validation on AIRSAR Dataset

ROC curves in the selected AIRSAR image are shown in Figure 14. Tables 8 and 9 independently show the AUC of PPLA and the AUC of SVM. There is little difference between the model-based approaches in the ROC curves owing to the high TCR of the measured data. The results indicate that the proposed method can work effectively and is applicable to AIRSAR Dataset.

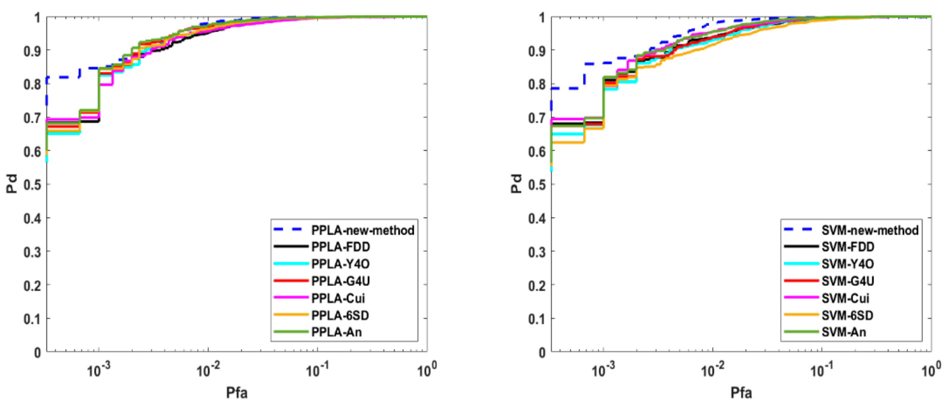

(**a**) (**b**)

Figure 14. ROC curves of different decomposition methods in the AIRSAR image. (**a**) ROC curves of PPLA; (**b**) ROC curves of SVM.

Table 8. AUC of PPLA.

PPLA	AUC
new method	0.9985
An	0.9985
G4U	0.9982
6SD	0.9981
Y4O	0.9978
FDD	0.9976
Cui	0.9972

Table 9. AUC of SVM.

SVM	AUC
new method	0.9977
An	0.9976
Cui	0.9973
G4U	0.9970
FDD	0.9965
Y4O	0.9965
6SD	0.9951

Figures 15 and 16 visually show the decomposition results of our decomposition model in RS-2 and AIRSAR respectively. Please enlarge the images to see the targets clearly. The scattering powers are color-coded as blue for P_{s}, green for P_{v}, and red for P_{d}. As indicated in Figures 15b and 16b, the water body appears blue. This demonstrates that water body represents well-expected surface scattering phenomena in the proposed decomposition method. Furthermore, in Figure 15b, the power P_{d} of the double-bounce scattering is particularly strong in areas near the ships. However, in Figure 16b, the double-bounce scattering power P_{d} is particularly strong in clutter areas. To find out why the proposed decomposition model can work effectively in the actual scene, we decompose the coherency matrices of targets and clutter.

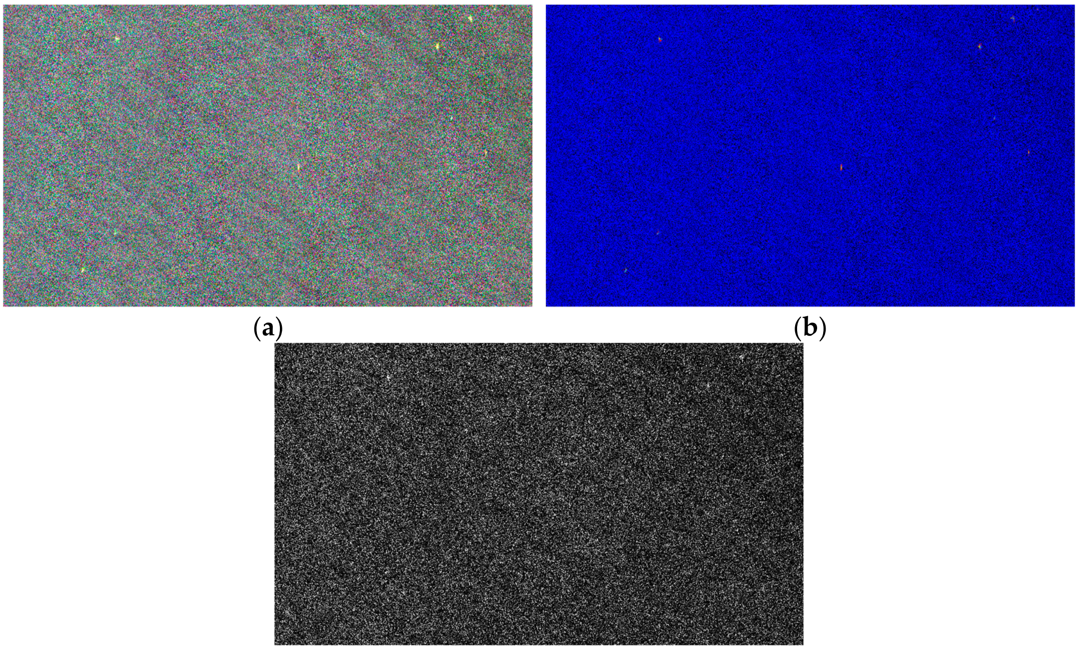

Figure 15. Decomposition results of the proposed decomposition model in the RS-2 image. (**a**) Selected RS-2 image; (**b**) The RGB color-codes: blue: Odd, green: Vol, red: Dbl; (**c**) Scattering power P_{od}.

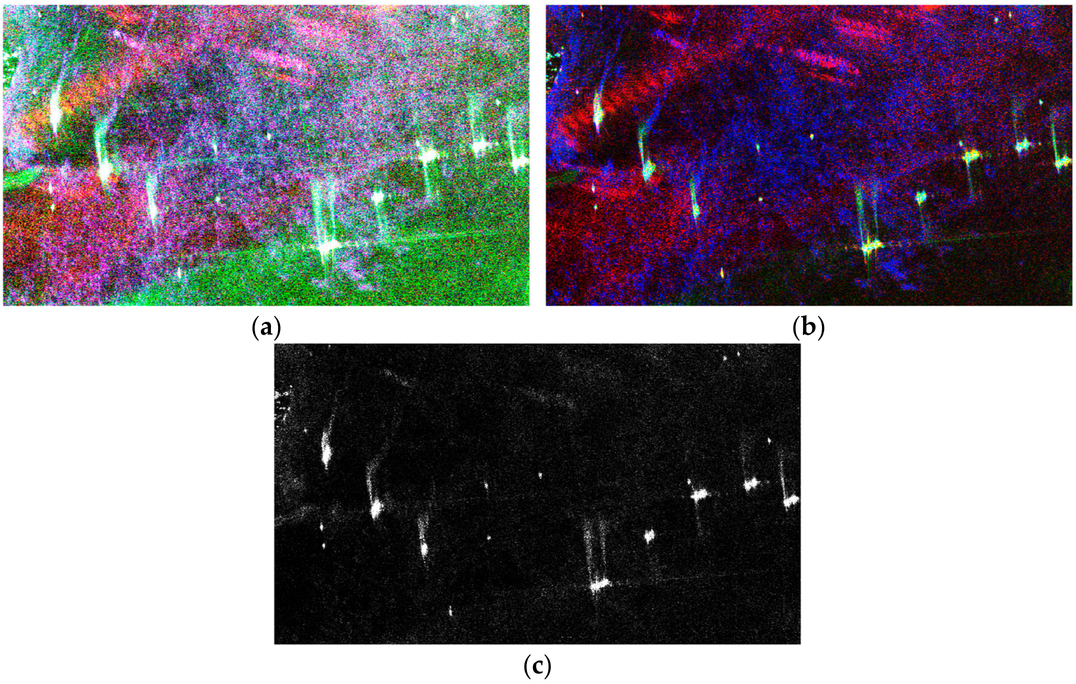

Figure 16. Decomposition results of the proposed decomposition model in the AIRSAR image. (**a**) Selected AIRSAR image; (**b**) The RGB color-codes: blue: Odd, green: Vol, red: Dbl; (**c**) Scattering power P_{od}.

Figure 17 displays the relationship between the normalized relative ratio of targets and the normalized PPLA weight in measured data. The specific values are listed in Tables 10 and 11. It is not difficult to see from Figure 17 that the larger the relative ratio of targets, the greater the weight of PPLA. It can be seen clearly in Table 10 that the third row is the normalized ratio of targets over clutter and P_d is dominant. Correspondingly, the PPLA weight of P_d is the largest. This means that the measured results are in accord with the results of simulated data. As shown in Table 11, P_{od} is dominant and the PPLA weight of P_{od} is the largest. This is because simulated data are generated based on RS-2 and the AIRSAR image is different from the RS-2 image. In Figure 16c, the importance of the scattering P_{od} is demonstrated and the effectiveness of our decomposition method is further validated.

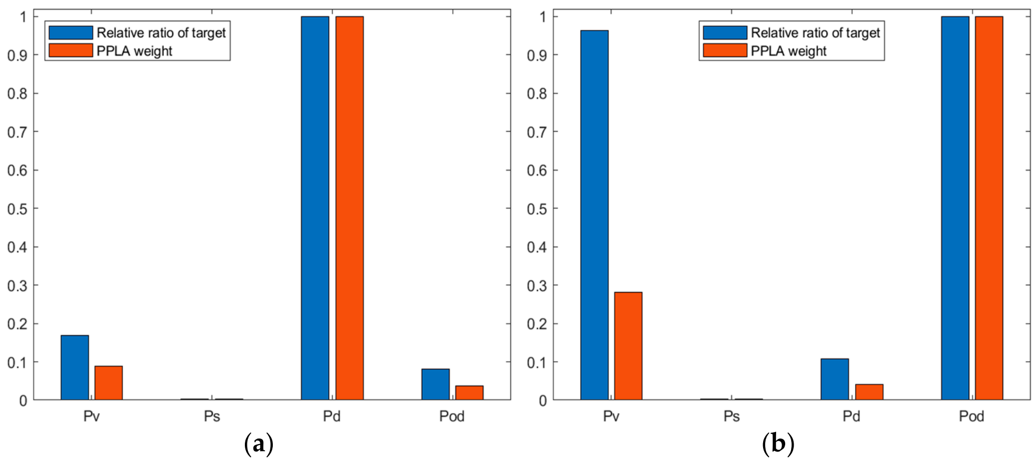

Figure 17. PPLA weight and relative ratio of targets in measured data. (**a**) RS-2; (**b**) AIRSAR.

Table 10. The percentage and PPLA weight of each component's power in measured data (RS-2).

Scattering Power	P_v	P_s	P_d	P_{od}
Targets decomposition percentage	8.2121%	45.1291%	35.7865%	10.8723%
Clutter decomposition percentage	4.2888%	82.5320%	4.1453%	9.0339%
Relative ratio of targets (normalization)	0.1692	0	1	0.0812
PPLA weight (normalization)	0.0878	0	1	0.0374

Table 11. The percentage and PPLA weight of each component's power in measured data (AIRSAR).

Scattering Power	P_v	P_s	P_d	P_{od}
Targets decomposition percentage	24.4080%	30.5609%	32.6345%	12.3966%
Clutter decomposition percentage	18.1150%	36.4008%	36.4129%	9.0713%
Relative ratio of targets (normalization)	0.9636	0	0.1074	1
PPLA weight (normalization)	0.2809	0	0.0408	1

In summary, the results of the proposed four-component decomposition method are consistent with the actual scattering mechanisms. The proposed four-component decomposition model can be applied to real applications.

4. Discussion

In this paper, a novel four-component decomposition method applicable to ship detection is proposed. In order to evaluate the detection performance of the proposed method, we conduct experiments on RS-2 data and AIRSAR data.

The results of simulated experiments show that no matter how the detection background changes, the proposed four-component decomposition can always achieve the best performance in the low-resolution case. It should be noted, in the high-resolution cases, the proposed decomposition method can also work well and does not achieve worse performance than other methods. For each simulated scene, the results from PPLA and SVM follow similar trends. Meanwhile, the proposed decomposition method is consistent with the real scattering mechanisms as well as the physical meaning of power. In addition, we also find that the larger the relative ratio of targets, the greater the weight of PPLA. This is why our four-component decomposition model can work effectively.

5. Conclusions

This paper intends to explore whether a model-based polarimetric decomposition method exists that can work effectively under different detection backgrounds. Firstly, the Lasso technique was adopted to select four types of features from 23-dimensional features which were composed of six polarimetric decomposition methods. Then, a four-component decomposition model was proposed based on the obtained feature components, i.e., surface scattering component (Odd), double-bounce scattering component (Dbl), volume scattering component (Vol), and $\pm 45^\circ$ oriented dipole component (Od). Additionally, PPLA and SVM were applied to solve the linear inseparable problems. Lastly, by using both simulated data and measured data, we compared the proposed four-component decomposition method with six kinds of conventional decomposition methods such as FDD, Y4O, G4U, and so on. From a comparison of the experimental results, it is evident that the proposed method is suitable for ship detection in different complex scenes. In the case of low resolution, the proposed method works better than other decomposition methods. In high-resolution cases, the proposed method does not achieve worse performance than other decomposition methods used in this paper. In addition, the proposed four-component decomposition model is consistent with the actual scattering mechanism and can be applied to real applications with potentially great benefits.

This study provides a confirmation of the applicability of machine learning to the model-based POLSAR decomposition topics. In the future, the next focus will investigate interpretable deep learning technology applicable to ship detection in POLSAR imagery.

Author Contributions: Conceptualization, L.F. and T.L.; methodology, L.F.; software, L.F.; validation, L.F.; formal analysis, L.F.; investigation, L.F.; resources, L.F.; data curation, L.F.; writing—original draft preparation, L.F.; writing—review and editing, L.F., T.L., Z.Y. and W.M.; visualization, L.F.; supervision, T.L.; project administration, T.L.; funding acquisition, T.L. All authors have read and agreed to the published version of the manuscript.

Funding: This research was funded by the National Natural Science Foundation of China (Grant No. 62171452).

Data Availability Statement: The data used to support the findings of this study are available from the corresponding author upon request.

Conflicts of Interest: The authors declare no conflicts of interest.

References

1. Brekke, C.; Anfinsen, S.N. Ship Detection in Ice-Infested Waters Based on Dual-Polarization SAR Imagery. *IEEE Geosci. Remote Sens. Lett.* **2011**, *8*, 391–395. [CrossRef]
2. Cui, Y.; Yamaguchi, Y.; Yang, J.; Kobayashi, H.; Park, S.E.; Singh, G. On Complete Model-Based Decomposition of Polarimetric SAR Coherency Matrix Data. *IEEE Trans. Geosci. Remote Sens.* **2014**, *52*, 1991–2001. [CrossRef]
3. Gao, G.; Shi, G.T. CFAR Ship Detection in Nonhomogeneous Sea Clutter Using Polarimetric SAR Data Based on the Notch Filter. *IEEE Trans. Geosci. Remote Sens.* **2017**, *55*, 4811–4824. [CrossRef]
4. Liu, T.; Jiang, Y.N.; Marino, A.; Gao, G.; Yang, J. The Polarimetric Detection Optimization Filter and its Statistical Test for Ship Detection. *IEEE Trans. Geosci. Remote Sens.* **2022**, *60*, 1–18. [CrossRef]
5. Sciotti, M.; Pastina, D.; Lombardo, P. Polarimetric detectors of extended targets for ship detection in SAR images. In Proceedings of the IEEE 2001 International Geoscience and Remote Sensing Symposium (Cat. No.01CH37217), Sydney, NSW, Australia, 9–13 July 2001.
6. Yang, J.; Yamaguchi, Y.; Boerner, W.M.; Lin, S. Numerical methods for solving the optimal problem of contrast enhancement. *IEEE Trans. Geosci. Remote Sens.* **2000**, *38*, 965–971. [CrossRef]
7. Touzi, R. Target scattering decomposition in terms of roll-invariant target parameters. *IEEE Trans. Geosci. Remote Sens.* **2007**, *45*, 73–84. [CrossRef]
8. Zhang, T.; Ji, J.; Li, X.; Yu, W.; Xiong, H. Ship Detection from PolSAR Imagery Using the Complete Polarimetric Covariance Difference Matrix. *IEEE Trans. Geosci. Remote Sens.* **2019**, *57*, 2824–2839. [CrossRef]
9. Biondi, F. A Polarimetric Extension of Low-Rank Plus Sparse Decomposition and Radon Transform for Ship Wake Detection in Synthetic Aperture Radar Images. *IEEE Geosci. Remote Sens. Lett.* **2019**, *16*, 75–79. [CrossRef]
10. Cui, Z.; Li, Q.; Cao, Z.; Liu, N. Dense Attention Pyramid Networks for Multi-Scale Ship Detection in SAR Images. *IEEE Trans. Geosci. Remote Sens.* **2019**, *57*, 8983–8997. [CrossRef]
11. Zhao, Y.; Zhao, L.; Xiong, B.; Kuang, G. Attention Receptive Pyramid Network for Ship Detection in SAR Images. *IEEE J. Sel. Top. Appl. Earth Observ. Remote Sens.* **2020**, *13*, 2738–2756. [CrossRef]
12. Jin, K.; Chen, Y.L.; Xu, B.; Yin, J.J.; Wang, X.S.; Yang, J. A Patch-to-Pixel Convolutional Neural Network for Small Ship Detection with PolSAR Images. *IEEE Trans. Geosci. Remote Sens.* **2020**, *58*, 6623–6638. [CrossRef]
13. Ringrose, R.; Harris, N. Ship detection using polarimetric SAR data. In Proceedings of the CEOS SAR Workshop, Toulouse, France, 26–29 October 1999.
14. Chen, J.; Chen, Y.L.; Yang, J. Ship Detection Using Polarization Cross-Entropy. *IEEE Geosci. Remote Sens. Lett.* **2009**, *6*, 723–727. [CrossRef]
15. Krogager, E. New decomposition of the radar target scattering matrix. *Electron. Lett.* **1990**, *26*, 1525–1526. [CrossRef]
16. Cameron, W.L.; Youssef, N.N.; Leung, L.K. Simulated polarimetric signatures of primitive geometrical shapes. *IEEE Trans. Geosci. Remote Sens* **1996**, *34*, 793–803. [CrossRef]
17. Huynen, J.R. Phenomenological Theory of Radar Targets. Ph.D. Dissertation, Delft University of Technology, Delft, The Netherlands, 1970.
18. Yang, J.; Peng, Y.N.; Yamaguchi, Y.; Yamada, H. On Huynen's decomposition of a Kennaugh matrix. *IEEE Geosci. Remote Sens. Lett.* **2006**, *3*, 369–372. [CrossRef]
19. Freeman, A.; Durden, S.L. A three-component scattering model for polarimetric SAR data. *IEEE Trans. Geosci. Remote Sens.* **1998**, *36*, 963–973. [CrossRef]

20. Yamaguchi, Y.; Moriyama, T.; Ishido, M.; Yamada, H. Four-component scattering model for polarimetric SAR image decomposition. *IEEE Trans. Geosci. Remote Sens.* **2005**, *43*, 1699–1706. [CrossRef]
21. An, W.T.; Cui, Y.; Yang, J. Three-Component Model-Based Decomposition for Polarimetric SAR Data. *IEEE Trans. Geosci. Remote Sens.* **2010**, *48*, 2732–2739.
22. Lee, J.S.; Ainsworth, T.L. The Effect of Orientation Angle Compensation on Coherency Matrix and Polarimetric Target Decompositions. *IEEE Trans. Geosci. Remote Sens.* **2011**, *49*, 53–64. [CrossRef]
23. Yamaguchi, Y.; Sato, A.; Boerner, W.M.; Sato, R.; Yamada, H. Four-Component Scattering Power Decomposition with Rotation of Coherency Matrix. *IEEE Trans. Geosci. Remote Sens.* **2011**, *49*, 2251–2258. [CrossRef]
24. Singh, G.; Yamaguchi, Y.; Park, S.E. General Four-Component Scattering Power Decomposition with Unitary Transformation of Coherency Matrix. *IEEE Trans. Geosci. Remote Sens.* **2013**, *51*, 3014–3022. [CrossRef]
25. Lee, J.S.; Ainsworth, T.L.; Wang, Y.T. Generalized Polarimetric Model-Based Decompositions Using Incoherent Scattering Models. *IEEE Trans. Geosci. Remote Sens.* **2014**, *52*, 2474–2491. [CrossRef]
26. Singh, G.; Yamaguchi, Y. Model-Based Six-Component Scattering Matrix Power Decomposition. *IEEE Trans. Geosci. Remote Sens.* **2018**, *56*, 5687–5704. [CrossRef]
27. Chen, S.W.; Wang, X.S.; Xiao, S.P.; Sato, M. General Polarimetric Model-Based Decomposition for Coherency Matrix. *IEEE Trans. Geosci. Remote Sens.* **2014**, *52*, 1843–1855. [CrossRef]
28. Zou, B.; Zhang, Y.; Cao, N.; Minh, N.P. A Four-Component Decomposition Model for PolSAR Data Using Asymmetric Scattering Component. *IEEE J. Sel. Top. Appl. Earth Observ. Remote Sens.* **2015**, *8*, 1051–1061. [CrossRef]
29. An, W.T.; Lin, M.S. A Reflection Symmetry Approximation of Multilook Polarimetric SAR Data and its Application to Freeman-Durden Decomposition. *IEEE Trans. Geosci. Remote Sens.* **2019**, *57*, 3649–3660. [CrossRef]
30. Guissard, A. Mueller and kennaugh matrices in radar polarimetry. *IEEE Trans. Geosci. and Remote Sens.* **1994**, *32*, 590–597. [CrossRef]
31. Lee, J.S.; Pottier, E. *Polarimetric Radar Imaging: From Basics to Applications*; CRC Press: Boca Raton, FL, USA, 2009.
32. Cloude, S. *Polarisation: Applications in Remote Sensing*; Oxford University Press: London, UK, 2009.
33. Tibshirani, R. Regression shrinkage and selection via the Lasso. *J. R. Stat. Soc. Ser. B Stat. Methodol.* **1996**, *58*, 267–288. [CrossRef]
34. Anfinsen, S.N.; Doulgeris, A.P.; Eltoft, T. Estimation of the Equivalent Number of Looks in Polarimetric Synthetic Aperture Radar Imagery. *IEEE Trans. Geosci. Remote Sens.* **2009**, *47*, 3795–3809. [CrossRef]
35. Liu, T.; Yang, Z.Y.; Marino, A.; Gao, G.; Yang, J. Joint Polarimetric Subspace Detector Based on Modified Linear Discriminant Analysis. *IEEE Trans. Geosci. Remote Sens.* **2022**, *60*, 19. [CrossRef]
36. Liu, T.; Yang, Z.Y.; Gao, G.; Marino, A.; Chen, S.W. Simultaneous Diagonalization of Hermitian Matrices and Its Application in PolSAR Ship Detection. *IEEE Trans. Geosci. Remote Sens.* **2023**, *61*, 1–18. [CrossRef]
37. Liu, T.; Yang, Z.Y.; Marino, A.; Gao, G.; Yang, J. PolSAR Ship Detection Based on Neighborhood Polarimetric Covariance Matrix. *IEEE Trans. Geosci. Remote Sens.* **2021**, *59*, 4874–4887. [CrossRef]